Final Technical Report

Interfacing Massively Parallel Computers to Terabit Fiber Links

Grantee

The Regents of the University of California

University of California, San Diego

La Jolla CA 92093

August 1999

Principal Investigator: Sadik C. Esener
(619) 534-2723
~~534~~ 2732

Program Manager: Dr. A. Craig
(202) 767-4934

20000728 072

REPORT DOCUMENTATION PAGE

8

AFRL-SR-BL-TR-00-

0 3/4

1. AGENCY USE ONLY *(Leave blank)*	2. REPORT DATE	3.
		01 Aug 98 to 31 Jul 99 Final

4. TITLE AND SUBTITLE	5. FUNDING NUMBERS
Interfacing Massively Parallel Computers to Terabit Fiber Links	H16103 1651/01

6. AUTHOR(S)
Dr Sadik C. Esener

7. PERFORMING ORGANIZATION NAME(S) AND ADDRESS(ES)	8. PERFORMING ORGANIZATION REPORT NUMBER
The Regents of the University of California University of California, San Diego 9500 Gilman Drive La Jolla, CA 92093	

9. SPONSORING/MONITORING AGENCY NAME(S) AND ADDRESS(ES)	10. SPONSORING/MONITORING AGENCY REPORT NUMBER
AFOSR/NE 801 North Randolph Street, Rm 732 Arlington, VA 22203-1977	F49620-96-0309 *96-0309*

11. SUPPLEMENTARY NOTES

12a. DISTRIBUTION AVAILABILITY STATEMENT	12b. DISTRIBUTION CODE
Approved for public release, distribution unlimited	

13. ABSTRACT *(Maximum 200 words)*

This program investigated the potential use of refractive index modulation in III-V semiconductor multiple quantum wells for interfacing electronic parallel computers and/or local networks to terabit fiber links. The lack of efficient and fast optoelectronic devices capable of modulating large optical intensities inhibits such interfaces. Traditionally, multiple-quantum-well (MQW) devices have been limited to the use of amplitude modulation at low optical intensity. Although, the index modulation in MQW material is potentially higher than in other electro-optical materials, this effect is masked by the absorption leading to phase modulated devices with very high insertion loss. Thus the main thrust of this program was to study the refractive index modulation in III-V semiconductor MQW devices under high optical power. We have showed theoretically and experimentally during the course of this program, that the refractive index modulation in MQW materials although small in magnitude also exists above absorption saturation. This finding indicates the potential use of MQW material for phase modulation with low insertion loss when biased properly. A phase-shift interferometry method has been developed to measure the index change with a resolution of 1/2500. The measured index change in our MQW materials under intensity saturation was about 0.05% for a modulation voltage of 3V.

14. SUBJECT TERMS			15. NUMBER OF PAGES
			16. PRICE CODE

17. SECURITY CLASSIFICATION OF REPORT	18. SECURITY CLASSIFICATION OF THIS PAGE	19. SECURITY CLASSIFICATION OF ABSTRACT	20. LIMITATION OF ABSTRACT
UNCLASSIFIED	UNCLASSIFIED	UNCLASSIFIED	UL

TABLE OF CONTENTS

List of figures

Tables

1. Objectives and Accomplishments

The main objective of this program was to study the refractive index modulation in III-V semiconductor multiple-quantum-well (MQW) devices under high optical power. A secondary goal was to investigate the potential applications of this modulation in interfacing electronic parallel computers and/or local networks to terabit fiber links. Traditionally, MQW devices have been limited to the use of amplitude modulation at low optical intensity. Although, the index modulation in MQW material is considerably higher than in other electro-optical materials, this effect is masked by the absorption leading to phase modulated devices with very high insertion loss.

During the course of this program, we have showed theoretically and experimentally that the refractive index modulation in MQW materials although small in magnitude also exists above absorption saturation. This finding indicates the potential use of MQW material for phase modulation with low insertion loss when biased properly. A phase-shift interferometry method has been developed to measure the index change with a resolution of $\lambda/2500$. The measured index change in a MQW material under saturation is 0.047%.

In this report, we summarize the theory related to the refractive index modulation in MQW materials beyond absorption saturation, describe the phase-shift interferometry method, and detail the measurement results.

2. Theoretical Background

2.1 Refractive Index and Index Modulation in MQW Materials

Refractive index of a material is the macroscopic representation of light matter interaction when a photon field is passing through a medium. The interaction takes a form of photon absorption and re-emission by atomic dipole oscillators. When there is no energy loss in the passing photon field, the net result of the interaction is a phase delay represented by the refractive index. A permanent energy loss occurs when oscillators are excited to any higher energy states resulting from the absorption of photons. This usually occurs at the oscillator resonant energy. The refractive index is larger near the resonant energy as well because the light matter interaction is strongest at this energy.

The refractive index of a multiple-quantum-well (MQW) material represents its interaction with any photon passing through as well. The electron energy states are quantized in MQW material, and the resonant conditions occur at each quantized levels. The exciton (spatially bounded electron/hole pair) resonant energies are slightly below each quantized energy level. Corresponding refractive indices are higher near the exciton energy levels and photon absorption occurs at these levels. Thus there are specific energy levels corresponding to exciton oscillators, for which absorption and refraction in a MQW material can be associated with.

Absorption and index are coupled in an absorbing material through the Kronig-Kramers relation. Since the absorption coefficient in MQW material can be modulated electrically through the Quantum-Confined Stark Effect, the density of excitons is thus a function of applied electric field. Since the density of excitons also governs the refractive behavior of the material, the refractive index is also modulated by the electric field.

5
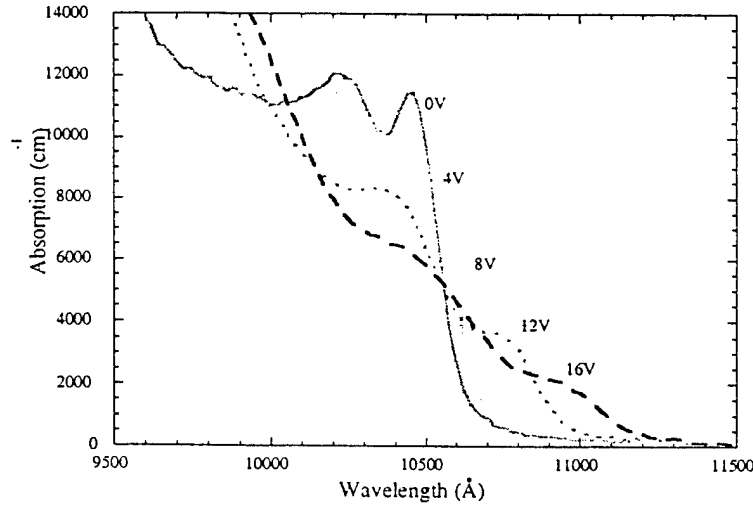
Figure 1: Low optical intensity electroabsorption spectrum for InGaAs/InAlGaAs MQWs. Notice the shift of the exciton absorption peak to longer wavelength with applied field. Broadening and reduction of absorption peak height also occur with applied field due to the reduction in electron-hole wavefunction overlap

The absorption coefficient spectra can be measured in function of applied-electric-field conditions. Figure 1 shows measured results in an InGaAs/InAlGaAs MQW material. Refractive indices can be calculated following the classical Kramers-Kronig relation. Figure 2 shows the calculated refractive index from the 0-V curve in Figure 1. Similarly, one can repeat the calculation for each curve in figure 1 and obtain the refractive index spectrum at each field condition. Figure 3 shows the calculated refractive-index spectra. The index modulation can thus be obtained with the applied electric field at a specific optical wavelength. For example, the expected index modulation is -0.01 at the 8-V applied voltage at the wavelength 1.064 μm.
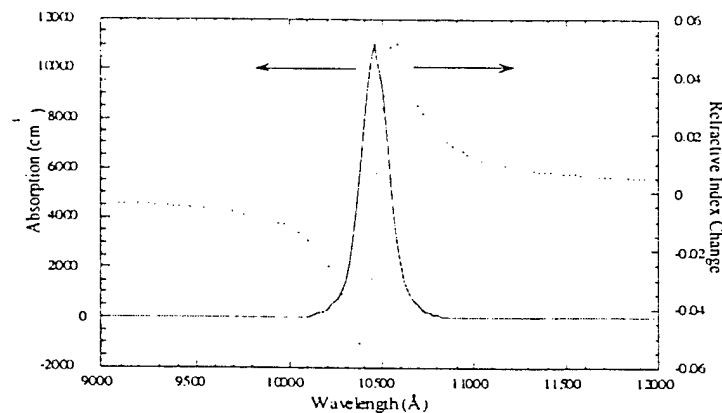
Figure 2: The measured exciton absorption resonance was isolated from the absorption spectrum (solid line), then its effect on the index as an isolated oscillator was estimated via a Kramers-Kronig transform (dashed line).
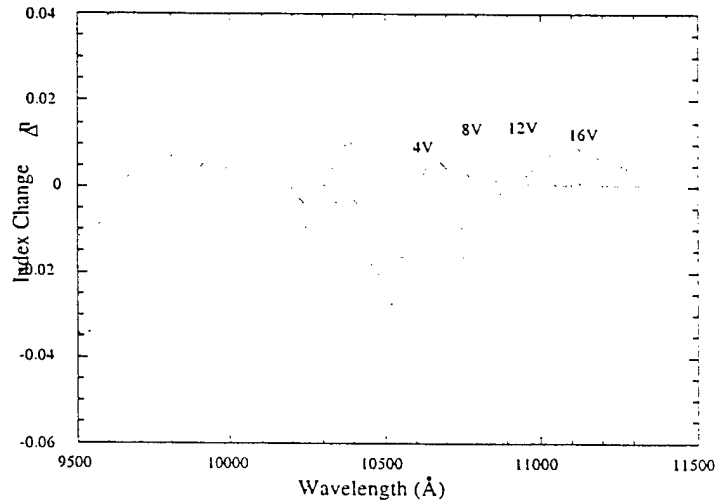
Figure 3: Electro-refraction spectrum estimated from the electro-
absorption spectrum through the use of a Kramers-Kronig
transform

However, in MQW materials, the exciton absorption can saturate at rather low intensities. It is then interesting to consider the refractive index of a MQW material where the exciton absorption is saturated. After the absorption is saturated, the material behaves more like a dielectric material with a constant refractive index. The value of this constant depends on the nature and the density of the oscillators. The density of exciton oscillators should be at its maximum when absorption is saturated, and the maximum value is a function of the absorption coefficient before the saturation.

2.2 Effects Related to High Carrier Density

Several phenomena occur when the absorption saturates in a material as a result of high concentration of photo-generated particles. They affect the absorption coefficient, the refractive index, aand/or the internal electric field. These effects are summarized below.

2.2.1 Bandfilling

At any given energy, there is a finite density of electronic states in the conduction and valence bands. Consider absorption at a wavelength just above the bandgap. Under low intensity illumination, there are ample electronic states available for electron transition to occur and hence, the absorption process in the material is not affected greatly. However, under high intensity illumination, many free carriers are generated and a finite number of electronic states are filled. Absorption coefficient, which is proportional to the number of available states, decreases in the material. At high enough illumination intensity, this bandfilling effect will reduce the absorption to zero, and the material will then become transparent. Further increases in the illumination intensity beyond saturation will no longer affect the absorption in the material.

7

The bandfilling effect increases the bandgap through the shift of the band edge to higher energies. Following the models described by Bennett *et al.*[1 and 2], the absorption change due to the bandfilling is negative for all cases at a fixed energy below the bandgap. This change in the absorption spectrum is coupled to a change in the refractive index described by the Kramers-Kronig relation. The calculated the refractive index is always negative as well, largest within a few meV of the band edge and approaching zero for $E \ll E_g$.

2.2.2   Bandgap Renormalization

The bandgap renormalization, also known as bandgap shrinkage, occurs when electron concentration is large enough. The electron wave functions will overlap, forming a gas of interacting particles. The electrons in the particle gas will repel one another by Coulomb forces. Also, electrons with the same spin will avoid one another due to the Pauli exclusion principle. This is can be thought of as each Fermion surrounded by a region where the probability for the existence of another identical Fermion is very small. Coulomb repulsion between equally charged Fermions, but not necessarily of the same spin, has a similar effect. The net result is a screening of electrons and a decrease in their energy, lowering the energy of the conduction band edge. A similar correlation effect for holes increases the energy of the valence band-edge. The result of these effects is bandgap shrinkage, which results in a red shift of the band edge. The effect on the index of refraction of bandgap renormalization is always positive, both above and below the band edge,[1,3] and is largest near the bandgap.

According to reference [25], the estimated shrinkage is proportional to the cube-root of the carrier concentration, i.e. the average inter-particle spacing. Correlation effects become significant when the inter-carrier spacing becomes comparable in size to the effective Bohr radius of the carriers. So, for low carrier concentrations, the bandgap renormalization effect is not significant. The change in index of refraction calculated from the Kramers-Kronig equation is positive below the bandgap.

2.2.3   Thermal Effects

Thermal effects arise in semiconductor optical devices primarily from resistive heating. This is directly related to carrier scattering resulting free carrier interactions with the crystal lattice[4]. Another thermal influence is non-radiative recombination of carriers, where a phonon rather than a photon is produced from carrier recombination. Normally, carrier sweep out rates, the rate at which carriers escape from the wells and are removed due to acceleration from the electric field, are much higher than recombination rates, so the former effect dominates in most cases.[5]

Thermal effects in semiconductors will increase the optical path length the photon field sees due to expansion of the lattice, shift the band edge, altering the absorption properties, and alter the carrier escape rates from quantum wells, since this process is dominated in MQWs with thick barriers by thermionic emission.

Increasing temperature in a semiconductor will reduce the bandgap. This shift of the band edge to lower energies translates into a positive change in the index of refraction at wavelengths near but below the band edge. Thermal effects on the index of refraction near the band edge can be quite large.[6] However, they are relatively slow for most device configurations.

8

2.2.4 Electric field screening

Electric field screening is caused by a charge build-up inside a material. In a photo-excited material, the charge build-up can result from the difference in electron and hole sweep-out rates, since each photon absorbed in a material generates an electron and a hole. It is the charge build-up of a single type of carrier in the quantum wells that leads to field screening. In MQW materials, electrons and holes escape from the quantum well via two main processes, thermionic emission and tunneling. Since electrons and holes have different masses and the energy barriers in a given material are not necessarily equal for both types of particles, the sweep-out rates are in general different for the two types.

Electric field screening is itself an electroabsorption process: the photo-generated carriers screen the applied electric field, which in turn induces a change in the absorption through the QCSE and the change in the index of refraction. In *p-i-n* modulators, charge can build up inside the quantum wells which can lead to an inhomogeneous electric field in the intrinsic region and a reduction of the depletion region of the diode.[7,9,10] The effect of space charge could inhibit the QCSE entirely at high optical powers.[6]

Calculations in references[8,9] show that under high intensity continuous illumination, only a fraction of the intrinsic region in the *p-i-n* diode experiences an electric field, as the depletion region is reduced from the charge build-up. The result is a reduction of the exciton red-shift produced by the external field, and exciton broadening. Both of these effects would change the absorption at the laser wavelength as the intensity increases.

Under steady-state conditions, field screening due to carrier build-up is considered the dominant physical mechanism determining the saturation of electrically biased MQW modulators in InP based material systems, which typically have high energy barriers for holes.[11]

3. Experimental Method

To measure the refractive index modulation above saturation intensity, a method of phase shift interferometry was used. To avoid the thermal effect, a pulse laser with picosecond pulse duration was used in the experiment. The interference fringes were generated by a wedged sample of surface-normal reflection-mode modulator. Interference fringes in the optical window of the MQW modulator were magnified, imaged onto a CCD, and captured by a computer. Then, the phase of the fringe pattern was determined row by row in the image through Fourier analysis. Fringe phases were compared between pairs of images captured with the modulator in the biased and unbiased states. The change in the index of refraction between these two states could then be calculated from the measured phase change.

3.1 Sample Preparation

The material used in these experiments was designed to operate at wavelengths compatible with commonly available high power lasers, such as YAG and YLF lasers, near 1.064μm. InGaAs/InAlGaAs quantum well material can be grown on GaAs wafers to show an exciton resonance at the desired wavelength. For operation at or near 1.06μm, however, the indium concentration in the InGaAs well material must be near 20%. This represents close to a 2% lattice mismatch with respect to the GaAs substrate. Strain relief occurs in the form of dislocations that propagate to the surface, degrading

device performance. Buffer layers can mitigate strain effects caused by the lattice mismatch. Such layers are grown underneath the quantum well material to gradually change the lattice constant to that of the well material. As has been demonstrated, the techniques of using linear graded, step graded, and superlattice buffers have been effective in filtering the threading dislocations generated from the lattice mismatch.[12,13] The buffer layers prevent a majority of the threading dislocations from propagating up through the material and into the active device layers.

PIN diode modulators were fabricated in the epitaxial layers on the front surface of the GaAs wafer sample using common lithographic and wet etching techniques. The backside of the sample was mechanically polished with an intentional wedge to generate interference fringes at a particular spatial frequency. Then a high reflectivity (at near-IR wavelengths) gold mirror was thermally evaporated onto the backside of the sample. The result is a reflective mode surface normal MQW modulator with an internal cavity to generate interference fringes.

The MQW material was processed into PIN ring diodes, with an optical window in the center of a ring contact. See Figure 4 for a diagram of the diode structure. Wet etch mesa isolation was used to electrically separate the modulators. A common ground
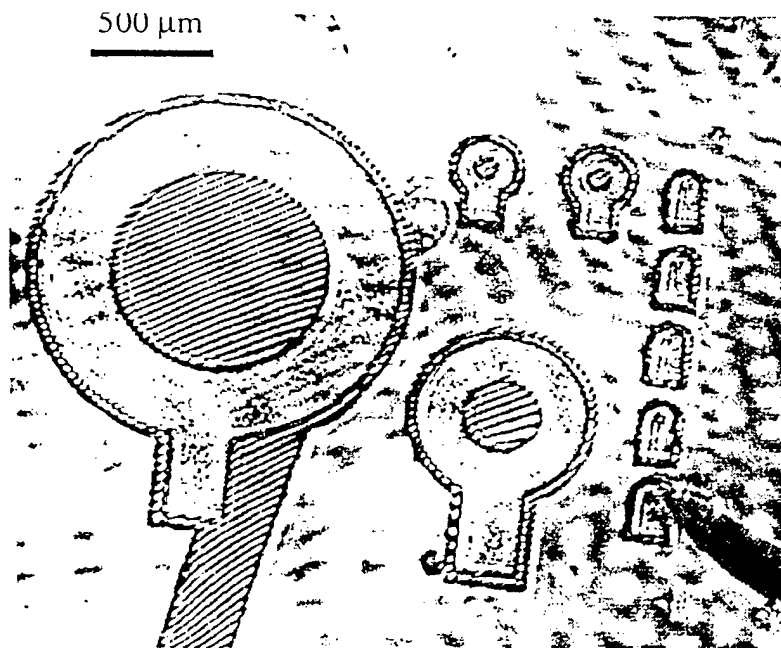
Figure 5: Several sizes of ring diodes fabricated on the InGaAs/InAlGaAs MQW material. Coherent illumination readily shows the straight interference fringes generated in diode windows due to the sample wedge angle. An electrical probe tip is visible at the lower right. The straight bar leading into the large size modulator is a break in the ground plane metallization caused by shadowing of the sample holder clip during the metal evaporation. Interference fringes can be seen in this area as well as the diode windows

10

plane, the p-doped buffer layers, was used for one electrical contact. The other contact, the n-doped cap layer, was located on top of the mesa. A typical lithographic and wet etching procedure was used to fabricate the devices. Electrical contacts were made using annealed AuGe and CrAuZn metallization.
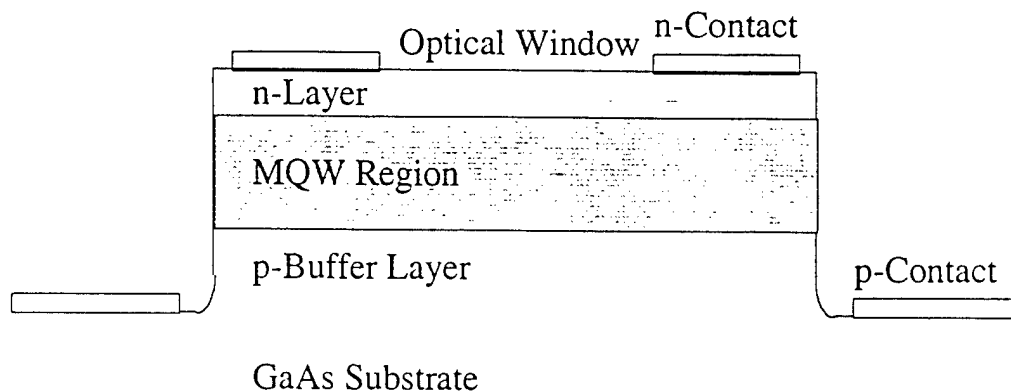
Figure 4: Cross-section view of the PIN modulator

The ring diodes were fabricated in several sizes on the sample, as can be seen in Figure 5. This image was formed with coherent illumination at 1064nm. The straight interference fringes due to the wedged sample are easily seen in the ring diode windows. The front surface of the modulator has a reflectivity of roughly 30% from the air-semiconductor interface, which interferes with the light returning from the back reflector. The wedge between the two surfaces generates straight interference fringes when the device is illuminated with coherent light.

The fringe phase determination method, which is described in detail below, requires approximately 10 fringes to obtain an accurate measurement[14]. So, the optical window of a single modulator must contain around 10 interference fringes. The mask set used to fabricate the diodes had several different sizes of diodes. However the intermediate size, with an optical window diameter of 275μm, was chosen as a target size for the 10 fringes. This ensured that extreme magnification would not be required in the experimental setup described below. Very high magnification, necessary for a smaller diode, would have made the measurement especially sensitive to vibration noise and unduly complicated the optical setup.

In order to ensure a fringe spacing of 27.5μm to fulfill the 10-fringe requirement, the backside of the sample was polished with a wedge angle of approximately 0.6°. The wedge angle can be derived from the desired fringe spacing (10 fringes per 275μm) and the phase change for one complete fringe (2π). The wedge angle can be found using the relation

$$\theta = \tan^{-1}\left[\frac{N\lambda_f}{x}\right] \qquad (1) \qquad\qquad \text{where}$$

$\lambda_f = \lambda_o/n$, λ_o is the free space wavelength of light and n is the index of refraction of the wedge material, x is the total length of the fringes, N is the number of fringes, and θ is the wedge angle as in Figure 6.

The accuracy of the wedge polishing process was optically monitored with the sample mounted on the polishing chuck. Adjustments to the process could then be made with a minimum of handling of the device. The optical monitoring process involved flood illuminating the sample with coherent light from the expanded beam from a diode

Figure 6: Geometry of an optical wedge

pumped CW YLF laser operating at a wavelength of 1053nm. Then the reflected fringe pattern was magnified and imaged onto a CCD where the interference fringe spacing was noted. This method was used to verify that the desired fringe spacing was achieved.

After the polishing procedure was completed, a high reflectivity gold mirror was thermally evaporated onto the back surface. Approximately 2000Å of gold was evaporated onto 50Å of chromium used as a sticking layer.

3.2 Measurements

Two sets of experiments were taken. First, photocurrent measurements were performed to estimate the saturation intensity for the MQW diodes. Then, a high precision phase shift measurement were made to directly measure the change in index of refraction in the MQW layers under high intensity pulsed operation. A Fourier analysis was performed on captured fringe images to determine their phase. Changes in phase, and hence index of refraction, were found by comparison of the biased and unbiased states of the MQW modulator while the optical input intensity was well beyond the saturation limit. Several averaging techniques as well as a simple statistical analysis method were employed to reduce noise and give an estimate of the significance of the results.

3.2.1 Photocurrent Measurements

The measurements were performed under pulsed optical input to determine the saturation power of the MQW modulator under different bias conditions. The photocurrent was monitored as a function of input optical intensity and applied bias. The low intensity linear unsaturated regime and high intensity saturated regimes are clearly delineated.

Using the largest size diode on the MQW sample, window area 0.484 mm^2 (see Figure (15)), the current generated from the 10Hz, 35ps laser pulses was measured with a high-resolution ammeter. A Hewlett-Packard Model 3457A digital multimeter with

nanoamp resolution was used. The DC current setting of the instrument was used, and the photocurrent generated in the reverse biased diodes from the short laser pulses was enough to register on the ammeter on its most sensitive (nA) scale. By using the DC setting, the value measured is the integrated current over the sampling period of the ammeter. This approach does not quantify the high-speed characteristics of the current pulse, however it does provide a useful measure of photocurrent saturation.

In order to estimate the saturation intensity for the measured photocurrent curves, the data was fitted with a Lorentzian saturation equation, $1/(1+I/I_s)$, in the form of

$$I_{abs}(V) = \frac{I_i k(V)}{1 + \dfrac{I_i}{I_s(V)}} \qquad (2)$$

where I_i is the incident optical intensity and I_s is the saturation intensity. The $k(V)$ parameter is related to the absorption coefficient at low optical intensity α_o, the absorption length of the modulator material L, and the modulation voltage V through $k(V) = 1-\exp[-\alpha_o(V)L]$.[15]

The measured data is shown in Figure 7 along with fits to the experimental data using Equation (2).
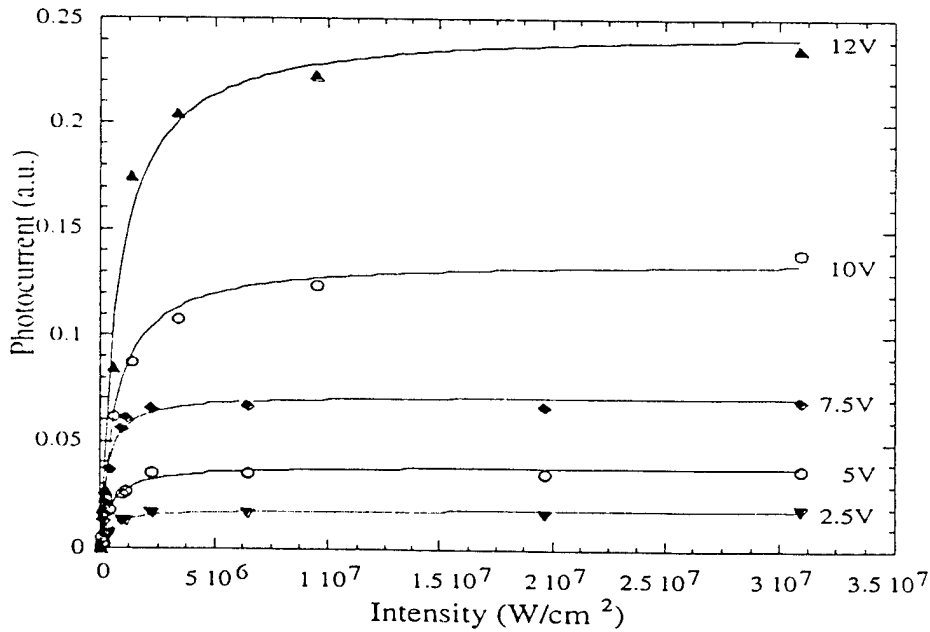

Figure 7: Photocurrent saturation characteristics with pulsed laser input

13

Table (1) Saturation intensities for optical excitation with 35ps laser pulses

Applied Voltage (V)	I_s (kW)	I_s (W/cm²)
2.5	.088	3.0×10^5
5	.173	4.4×10^5
7.5	.407	4.7×10^5
10	.501	7.0×10^5
12	.653	7.9×10^5

Table 1 lists values for I_s found from the curve fits to the experimental data. Saturation-intensity increasing with applied bias is evident. This suggests faster carrier sweepout from lowered barriers from the electric field. Values of I_s from 100 to 632 kW/cm² have been observed by several sources for similar InGaAs/GaAs MQW materials.[12,16] The results presented here are in line with those reported values. These values are considered in the high range for MQW absorption modulators. High saturation intensities can be attributed to fast carrier escape rates and/or fast recombination times. MQW materials with a high density of dislocations from strain relaxation tend to have low quantum efficiencies due to carrier recombination at dislocation sites in the wells. This fast recombination decreases the effective carrier lifetime, so modulators with higher dislocation densities tend to have higher saturation intensities.

3.2.2 Interference Fringe Shift Measurement

This section describes the experimental setup and procedures used to measure the change in index of refraction in the modulator through fringe shift interferometry. Allowing for averaging and statistical analysis techniques, the measurement technique provides for a minimum detectable phase shift on the order of $\lambda/1000$ with a sample size of 50, and $\lambda/2500$ or better with larger sample sizes.

The technique, which directly measures the change in the index of refraction from an electroabsorption saturated MQW modulator, uses a reflective modulator fabricated to produce interference fringes within the optical window of the active device. The fringes are imaged onto a CCD and are captured with and without an applied electrical bias on the modulator. The phase shift of the interference fringes between the biased and unbiased conditions is then measured with a Fourier analysis of each fringe pattern. The change in index of refraction in the modulator can then be determined once the phase shift is known.

This technique for direct measurement of the change in the index gives the sign as well as the magnitude of the change. It thus yields significant clues to the physics supporting the experiment. This hopefully validates and simplifies the interpretation of the experimental results.

3.2.2.1 Optical Setup

The optical setup used in these experiments was designed with several requirements in mind. The imaging system needed to deliver variable optical power to the diode modulator. The modulators were electrically probed, so a variable

magnification system was necessary. The sample is aligned into the system and electrically probed under low magnification. The magnification is then increased so that the fringe pattern in the diode window completely fills the CCD, giving the highest pixel count per complete fringe. A high degree of mechanical stability was also required since the fringe shift measurement is sensitive to vibrations.

The interference fringe generation method used in these experiments did not rely on two external mirrors to generate the interference fringe pattern. A typical external mirror interferometric setup, such as a Twyman-Green interferometer, can be quite sensitive to vibrations and air currents, as well as slow shifts in the positions of the optical components. For this reason, the interference fringes were generated through a wedge fabricated into the MQW sample during a polishing procedure. This eliminates several optical components from the interferometer, and guarantees greater stability since the two reflecting surfaces of the interferometer (the front and back of the MQW sample wafer) cannot move relative to each other.

The laser used in these experiments was a Continuum PY61C pulsed YAG laser. It generates 35ps pulses at a 10Hz repetition rate. The laser pulse was measured to have a tophat intensity profile. Thus there is a relatively constant intensity across the laser spot, as compared to a typical Gaussian intensity profile.
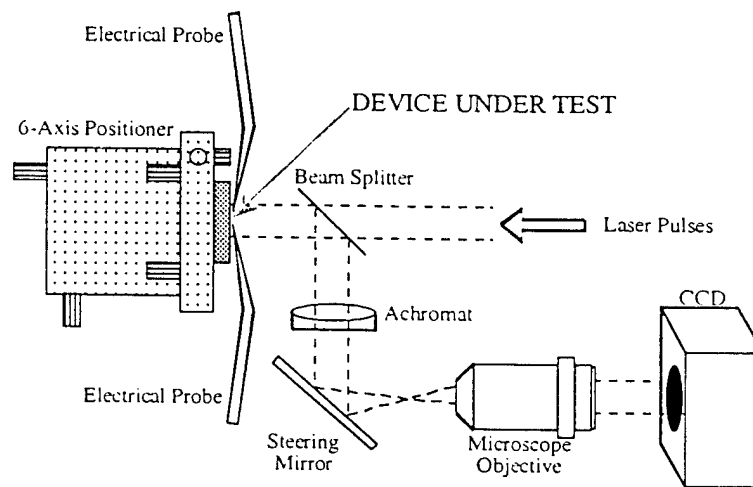
Figure 8: Layout of optical setup used in the precision fringe shift measurement

The optical setup used in the phase shifting experiments is diagrammed in Figure 8. Since the MQW modulator samples needed to be probed electrically, an optical system with variable magnification for fringe shift data collection and ample working distance was necessary to allow for electrical probing of the device. The modulators were probed under low magnification; then the fringes were imaged under higher magnification. Hence the imaging system consisted of an achromat lens with a focal length of 14cm, use in a 2f-imaging configuration and a microscope objective at the image plane of the achromat lens.

15

Variable magnification could be obtained by simply moving the achromat lens closer to or further away from the sample. This changes the size, as well as the position of the image generated by the achromat. During these experiments, the achromat was generally positioned for a magnification in the range of 1x to 3x. Thus, with a 5x or 20x microscope objective positioned at the achromat's image plane, magnifications from 5x to 60x could be obtained. This approach has the advantage of a large working distance to the sample for the electrical probes and steering optics.

The camera used to capture the fringe images was a Princeton Instruments Model TE/CCD-1317-K/1. This 16 bit camera uses a cooled CCD, operating temperature of 10°C, with 1316x1034 pixel resolution. The camera is controlled via a Macintosh computer and IPLabSpectrum image processing software from Signal Analytics.

The MQW modulator sample was mounted on a six-axis positioner: XYZ, pitch, yaw, and rotation. The MQW sample was probed electrically using micro-positioners and standard 25μm probe tips. The probes were connected via 50 ohm coaxial cable to a HP E3631A DC variable power supply and a HP 3457A current meter. The current meter was used in this experiment to verify electrical contact had been made with the probes and to monitor the I-V characteristics of the diode before and after the fringe shift experiment.

3.2.2.2 Data Collection Technique

During the measurement, the modulator sample is flood illuminated with 35ps 10Hz YAG laser pulses. The laser used could provide ample optical power in order to operate the MQW modulator well beyond its continuous wave (CW) absorption saturation point. The YAG laser was used at an average power output of 300mW. With a measured laser spot size of 13.2mm in diameter, this translates into a pulse intensity of $6x10^8$ W/cm^2.

A typical CW saturation intensity for a MQW modulator is on the order of 10^5 W/cm^2,[17] so there is ample optical power available from this laser, even when unfocused. The pulse intensity is adjusted so the device is biased beyond saturation at the highest applied voltages. The saturation limit was determined through monitoring of the photocurrent as was described above in the section related to photocurrent measurements.

The CCD camera used to capture the fringe patterns generates 16 bit resolution 1034x1316 pixel images. However, to speed data collection and image processing, and to keep the computer file storage manageable, images sizes of 100x1316 pixels were collected.

Since the shift in the phase of the fringes was expected to be small and the optical magnification used to image the fringes was fairly large, the data collection technique was sensitive to noise. One type of noise is physical vibration of the measurement system. There are various sources for vibration noise, including ground vibrations, air currents swirling around the optics from the ventilation system or audible noise, such as talking or music, creating pressure waves.

Sources of noise other than vibration include the thermal stability of the laser, thermal stability of the laboratory (heating and AC), laser pulse intensity variation, pointing

stability of the laser, stray light entering the camera, and component drift. Component drift occurs when the mounting hardware for an optic, or any component in the system, settles after being moved or tightened in place. This is generally a longer term drift type of noise and its effects can be reduced by waiting for settling to occur after the last adjustment is made before taking data. Fast data collection will also reduce drift noise since it is a slow process.

These noises sources were systematically reduced or eliminated as they were identified. Vibration noise was reduced through the use of stable mounting hardware. The experiments were done late at night to avoid traffic related ground vibrations. The system was enclosed to eliminate any noise from air currents. Laser thermal stability was increased with a nitrogen purge into the laser cavity and long warm-up times. The laboratory ventilation was turned on continuously and experiments were performed only after a stable room temperature was reached.

Each 100x1316 pixel image captured in these experiments represents a 650ms exposure. Thus there are six optical pulses integrated into each image, given the laser's 10Hz rep rate. This multiple pulse integration technique was used to reduce the effects of any intensity variation from pulse to pulse.

Images were captured in groups of 50 via automated image acquisition. Each set of 50 images took approximately 3 minutes to gather. This automated approach was taken to speed data collection in order to reduce error from component drift. While every effort was taken to minimize shifting of the image of the fringes on the CCD due to reasons other than a change in the index of refraction of the sample, it was found to be extremely difficult to eliminate all sources of error. However, the use of a fast data collection technique proved to be critical in bypassing slowly varying drift components of error.

3.3   Computer Analysis

The determination of phase shift between biased and unbiased states was performed after the fringe images had been collected. The analysis is a two-step process. First is the determination of the spatial frequency of the interference fringes for use in the next step, a Fourier analysis to determine the phase.

3.3.1   Spatial Frequency of Interference Fringes

In order to accurately determine the phase of the interference fringes, the spatial frequency of the pattern must first be determined. Recall that the sizes of the images captured on the computer were all 100 rows by 1316 columns. See Figure 9 for an example of a fringe image used in these calculations.

Figure 9: Image of interference fringes from wedged MQW diode optical window. The 16 bit images are 100 rows by 1316 columns

To accurately determine the spatial frequency of the fringes, a one-dimensional FFT was tperformed for each row of a single image. Thus 100 FFTs were performed. As a noise reduction technique the columns of the FFT data were summed. So a one dimensional FFT spectrum was obtained from the summation of the 100 FFTs from the entire image. Figure10 is an example of such a FFT spectrum.

To minimize error in the phase calculation, which is described in the next section, determination of the spatial frequency should be performed to an accuracy of ±0.1 or better.[47] The FFT function returns values at integer frequency intervals, so an interpolation is performed to find the frequency of the peak in the FFT data when it falls between integer values. In this manner, the spatial frequency of the interference fringe pattern is easily determined to within 0.1.

Note that the value of the spatial frequency is normalized to the length of the data set. That is, if there are 1316 pixels in each row, and there are 10 complete fringes in the image, the spatial frequency would be 10, with 131.6 pixels per complete fringe (2π phase change).

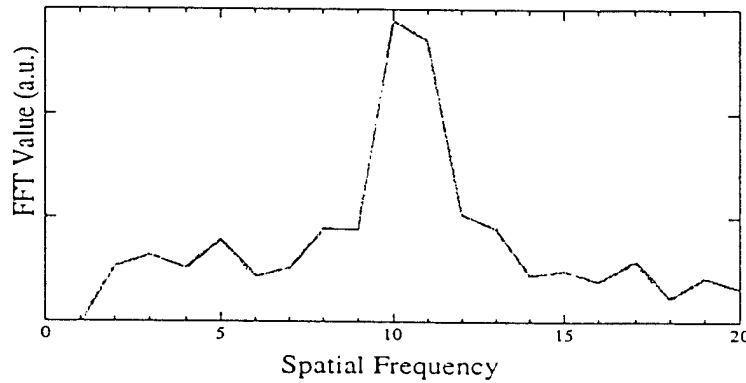Figure 10: FFT spectrum of interference fringes obtained by summation of FFTs from each row of the fringe image

3.3.2 Phase of Interference Fringes

The calculations performed to find the phase difference between two interference fringe images is described as following.

A profile of the interference fringes generated in the window of the MQW modulator can be written as

$$I_1(x) = W(x)[1 + \cos(2\pi fx - \phi_1)] \tag{3}$$

where x is the spatial coordinate, and f and ϕ_I are the spatial frequency and intrinsic phase of the fringes. The window function of the fringe pattern truncating the signal is represented by W(x). The fringe profile after applying a bias voltage (assuming there is an index change in the well material) can be expressed as

$$I_2(x) = W(x)[1 + \cos(2\pi fx - \phi_1 - \delta\phi)] \tag{4}$$

where the change in phase is represented by $\delta\phi$. Figure 11 shows a typical intensity profile taken from one row of a fringe image.

To find the phases of the interference fringes, the Fourier cosine and sine integrals are calculated as
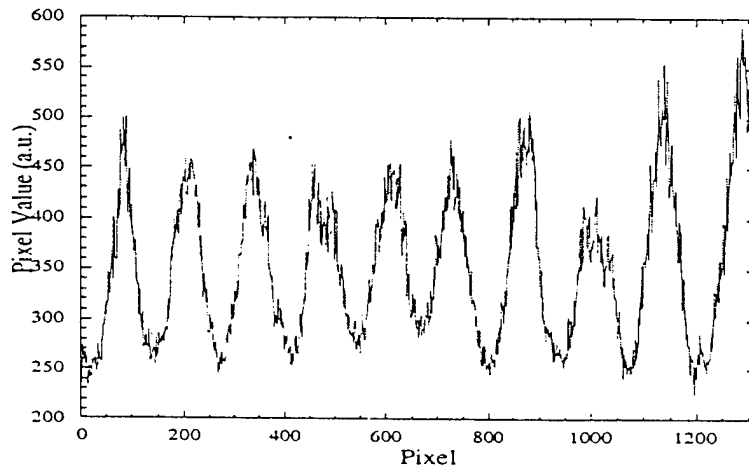
Figure 11: Fringe intensity profile of a single row of the interference image.

$$C_i = \int_0^1 I_i(x)\cos(2\pi fx)dx$$

$$S_i = \int_0^1 I_i(x)\sin(2\pi fx)dx \tag{5}$$

where the range of the fringes is normalized and i=1,2. From the Fourier sine and cosine functions the phase of the fringe pattern can be found with the arctangent function:

$$\phi_i = \tan^{-1}(S_i/C_i) \tag{6}$$

where ϕ_2 is actually $\phi_1+\delta\phi$. Therefore, the phase change can be found as the difference between the phases ϕ_1 and ϕ_2.[18]

There are 100 rows of fringe intensity data in each image captured by the computer. The phase of each row is found using the discrete version of Equation (6):

$$\phi = \tan^{-1} \frac{\sum_x I(x)\sin\frac{-2\pi f}{N}x}{\sum_x I(x)\cos\frac{-2\pi f}{N}x} \qquad (7)$$

where N is the number of pixels per row and the quantity $2\pi f/N$ is the normalized spatial frequency.

The procedure for computation of the phase difference between two interference fringe patterns is as follows. First, using Equation (7), the phase of each row of a baseline image is computed. Since images generated had 100 rows, 100 associated phases were computed. All subsequent images for that particular set of experimental data were compared to this baseline image.

Then, the same phase calculation is performed for each row of the next fringe image in the set. The phase difference is computed between the current image and the baseline image, row by row. For example, the phase computed from the first row of the baseline is subtracted from the phase of the first row of the current image, second from second, etc.... so 100 phase differences were found. Figure 12 shows such phase differences.
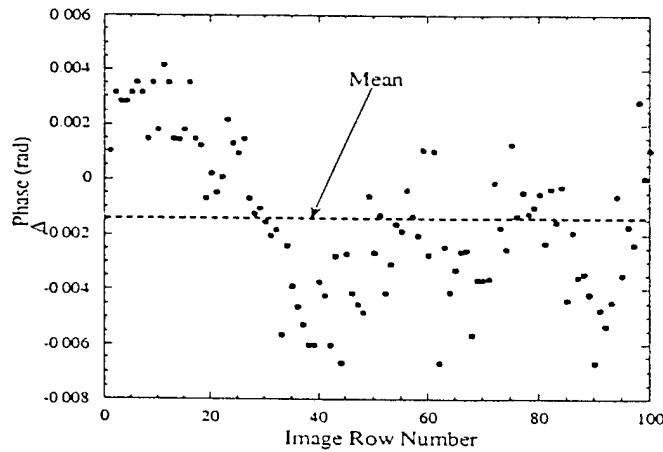
Figure 12: Phase differences calculated for two interference fringe images. The phase of each row in both images was calculated through Fourier sine and cosine integrals. Phase differences were found for each row in the images

As a final step in the determination of the phase shift between the two images, the average of all the phase differences is found. Thus the information contained in two high-resolution images is reduced to a single number.

Nakadate[14] used a similar method of analysis to measure phase shifts in a common path interferometer which used Young's fringe generation from a birefringent optical wedge and polarizing filter. He found that, using a CW laser source and a 12 bit resolution image sensor 256 pixels long, the minimum detectable phase shift was $\lambda/4000$ and the accuracy was $\sim\lambda/2000$.

As mentioned previously, the image sensor used in the experiments presented here is a 16 bit resolution 1316x1012 CCD. With 10 complete fringes imaged onto the sensor, there would be 131.6 pixels per fringe. This base resolution, in terms of pixels/fringe, is a factor of five better than in the Nakadate experiments. No averaging techniques were used by Nakadate.

Since the physical dimensions of the diode modulators were known, the spatial frequency of the fringe pattern could be found in terms of μm/fringe from an image of the interference fringes and an image of modulators features of known size taken at the same magnification. Using this method, the fringe spacing was estimated to be 35.0μm/fringe. A step size of 200nm was used with the computer controlled translation stage. This is a step of 0.57% of a full fringe, or 0.036 radians. While the translation stage was capable of 50nm steps, unresolved noise problems in the stepper drive or position encoder prevented the minimum possible step size from being used.

Gathering the data for this experiment, 50 images were saved with the translation stage at its starting position. The translation stage was then stepped 200nm and another 50 images would be acquired. The step and acquire was repeated several times.

After the images were captured for each position of the translation stage, they were processed using the computer analysis method described above. The analysis program reports the phase change of each image in relation to a reference image, which in each case is simply the first image acquired. The results from this experiment can bee seen in Figures (24) and (25). Plotted in Figure 13 is each phase shift data point. Each point represents the phase of the image relative to the first image acquired, sample number 0. The plot is broken up into sets of 50 images. Between each set of 50, the translation stage was stepped 200nm. Listed in Table 2 are the mean values of each of these sets of 50 data points, their standard deviations, and the differences between the means.
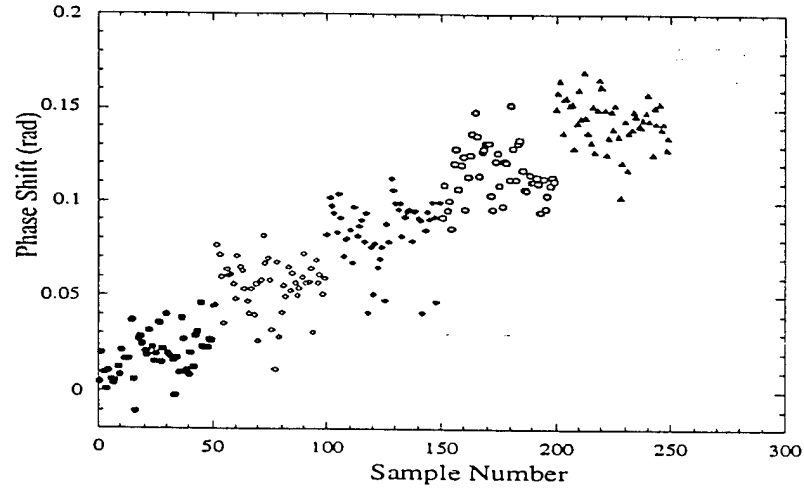
Figure 13:Phase shift data from the verification experiment. Each set of 50 data points were taken with the high-resolution translation stage at a fixed position. The stage was stepped 200nm between each set of data

Table (2). Values of the mean, deviation, and mean difference for each data set presented in Figure (13)

Data Set	Mean	Standard Deviation	Difference of Means
1	0.019	0.0110	
2	0.055	0.0137	0.036
3	0.084	0.0161	0.029
4	0.116	0.0143	0.032
5	0.144	0.0130	0.028
6	0.175	0.0153	0.031

The mean values from Table (2) are plotted in the following figure. The slope of the line fit (and the average of the mean differences) reveals a step size of 0.031 radians which is roughly $\lambda/200$. This compares well with the phase change estimated from the measured fringe spacing of 0.036 radians, a difference of only 16%. The linearity of the measurement is readily apparent from Figure 14.
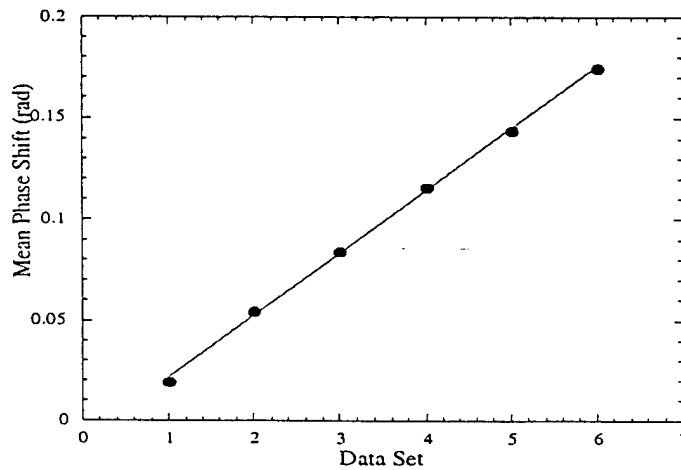
Figure 14: Plot of mean values of each data set of 50 points from Figure (13). A linear fit to the data is also shown

In order to determine the minimum detectable phase change, a common statistical analysis was performed on the data, the T-test. The primary purpose of the T-test is to determine whether the means of two groups of data differ to a statistically significant degree. Two data sets with different means may come from different groups of data, or the observed differences may have occurred by chance or sampling error.[19] The T-test helps determine which is the case.

A T-test is a test is, based on the means, standard deviations, and sample sizes of two data sets, returns a value which indicates the probability that the two samples are likely to have come from the same underlying population[20]. The function used in this evaluation returns a value of 1 if the two data sets are identical, and returns a value of 0 if the data set means are widely separated with small standard deviations. Values between 0 and 1 are returned for data sets whose means are close or that have large deviations.

A two-tailed T-test analysis assuming homogeneous variances was performed on two sets of 50 data points from Figure 13. The analysis was done in a spreadsheet application on a personal computer. The minimum detectable phase change was estimated by finding the separation of the means at which the T-test returned a value of 0.05. This indicates that there is a 95% probability that the two samples come from different populations, or a 5% probability that they come from the same population. The mean of one sample was brought closer to the mean of the other sample through addition of a constant to each data point in the set.

23

These tests reveal that the 95% confidence level is reached at a mean separation of .0062 radians, or $\lambda/1021$. So, with a sample size of 50 data points for each set, the resolution of the system is about $\lambda/1000$.

4. Experimental Results

From the phase shift interferometry measurement, groups of 50 data points were recorded for the biased and unbiased conditions. The input biases range from 2 to 12V. In the plot below (Figure 15), data points are presented for the unbiased (0V) state, the solid circles, and the biased (3V) state, the open circles. The input intensity is 1.4×10^7 W/cm^2, nearly two orders of magnitude higher than the measured traditional saturation intensity of 3×10^5 W/cm^2 (for a 2.5V bias).

While it is difficult to discern a signal by eye from the raw phase shift data, a plot of the mean values reveals the trend, Figure 16. The biased state shows a decrease in the mean value as compared to the unbiased. It is believed that data groups 15-17 were obtained in the presence of a slow drift noise source. This would explain the lower values obtained for these sets of data points.

A T-test analysis was performed on adjacent data groups. That is, groups one and two were tested, two and three, etc.. The results of this analysis are presented in Figure 17. Except for the tests 14 and 17 (for data groups 14/15 and 17/18), which do not indicate a significant difference, other seven tests show an 80% or higher confidence level. The average of all the (1 - T-test) values is 0.62.
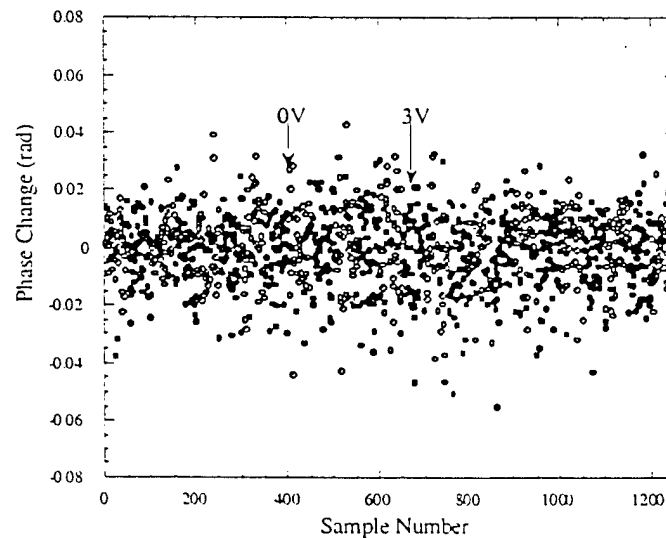

Figure 15: Phase shift data for 0V (closed circle) and 3V (open circle) bias. Data was collected in-groups of 50 for each bias condition, with 13 sets of 0V and 12 sets of 3V bias data being collected
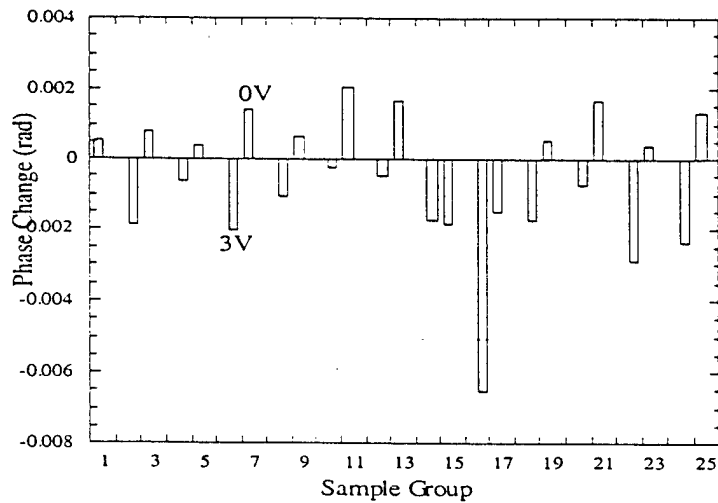
Figure 17: Mean for the groups of 50 data points presented in the previous figure. The solid bars represent the mean values for the biased states (3V) while the striped bars represent the unbiased state (0V)

As a further analysis of the data, the 0V means were separated from the 3V means. The mean of the means was then found for both bias states. This result is most simply presented (Figure 18) as two data points, with error bars representing the standard deviation of the mean of the means calculation. It is evident that there is indeed a measured shift in the phase of the interference fringe pattern. The difference in these values is found to be -0.0025 rad.
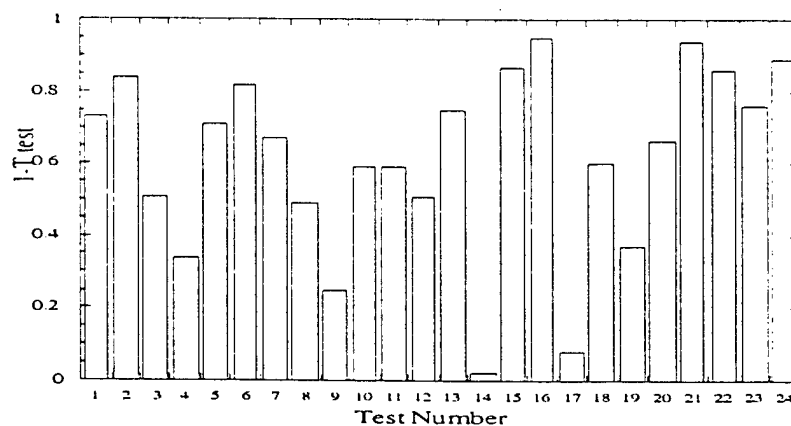

Figure 17: Results of a T-Test analysis on adjacent groups of phase change data. The value of (1-T-test) represents the probability that the two sets of data points come from different populations
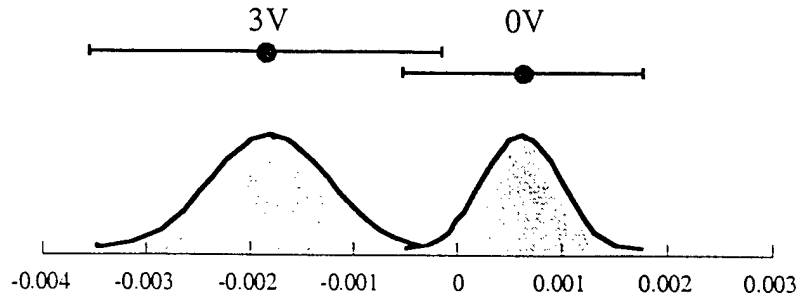
25

Figure 18: The mean of the means was computed for both the unbiased and biased state. Error bars represent the standard deviation. Gaussian curves representing normal distributions are included as an aid to the eye

The change in the refractive index can be calculated from the change in phase using by

$$\Delta\phi = 2\pi\frac{\Delta nL}{\lambda} \tag{8}$$

where L is the optical path length in the material thickness and λ is the wavelength of light. For a reflective modulator, the optical path length is double of the material thickness. From the measured phase shift $\Delta\phi$ of -0.0025 rad, the change in index is then -4.7x10^{-4}, using L=0.9μm and λ=1.064μm,

Compared to the calculated change in refractive index using Kramers-Kronig relation, Figure 19 (a) and (b), the measured change in refractive index is an order of magnitude smaller. One possible cause is the electric field screening in the modulator under high illumination. The data collected in the fringe-shift measurement for voltages higher than 3V do not show a statistically significant signal, within the experimental resolution. This is an indication of electric field screening. Unfortunately, due to the lack of tunable pulse laser of high power, the detailed dynamic behavior of the absorption and index of refraction could not be investigated.
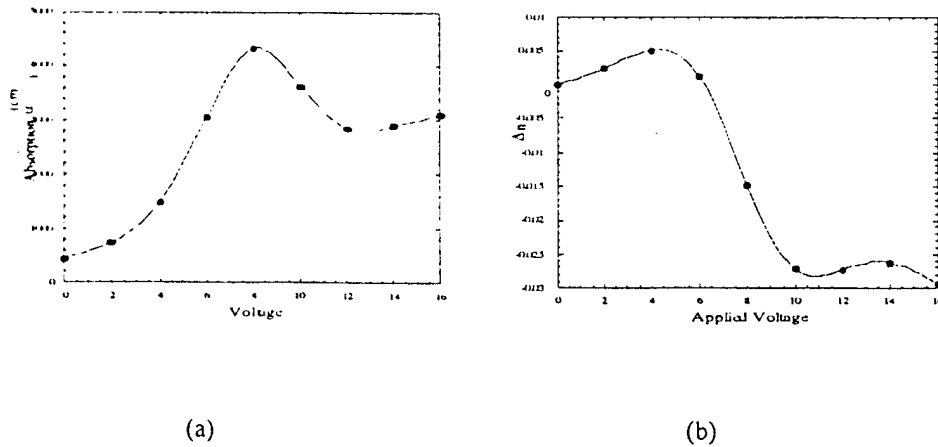

(a)   (b)

Figure 19: (a) Absorption and (b) index change for InGaAs/GaAs MQW modulators under low intensity illumination at 1064nm

26

5. Conclusion

We have demonstrated experimentally the refractive index modulation in MQW materials beyond the absorption saturation. The measured index change at high optical illumination is an order of magnitude smaller than estimated from the low-intensity absorption coefficient, which may indicate the presence of electric field screening under the high-intensity illumination.

As discussed in Section 2, the electric field screening is caused by the unbalanced escaped rates of electrons and holes in the wells. In general electrons are lighter than holes in any material, the screening is more likely caused by holes left in the wells. Therefore, the materials with higher potential barrier for electrons, such as GaAs related component materials, are better suited for the devices operating at high intensity. It has been reported that the incorporation of Nitrides in III-V semiconductor materials results in the increasing of conduction-band offsets in the MQW materials. Further research could be conducted in Nitride related materials if the MQW devices are to be used to modulate phase under high-intensity illumination.

Finally, the phase-shift interferometry method developed during the course of this work is proved to be a high-resolution technique to determine the index change in a material. It has the resolution of $\lambda/2500$.

6. Related Publications

C. Fan, B. Mansoorian, D. Van Blerkom, M. Hansen, V. Ozguz, S. Esener, and G. Marsden, " Digital free-space optical interconnections: a comparison of transmitter technologies," Applied Optics, Vol. 34, No. 17, 1995, pp. 3103-3115

M. Hansen, "High intensity phase modulation using absorption saturated multiple quantum wells." Ph.D. Dissertation, Electrical Engineering (Applied Physics), UCSD, 1998.

7. References

[1] B. R. Bennett, R. Soref, and J. Del Alamo, "Carrier-induced change in refractive index of InP, GaAs, and InGaAsP," IEEE Journal of Quantum Electronics, Vol. 26, No. 1, 1990, pp. 113-122

[2] A. Yariv, Optical Electronics, 3rd Ed. New York: Holt, Rinehart and Winston, 1985, pp. 474-478

[3] N. Peyghambarian, S. Koch, and A. Mysyrowicz, Introduction to Semiconductor Optics, New Jersey: Prentice Hall, 1993, p. 331

[4] G. Boyd, J. Cavaillès, L. Chirovsky, and D. Miller, "Wavelength dependence of saturation and thermal effects in multiple quantum well modulators," Applied Physics Letters, Vol. 63, No. 13, 1993, pp. 1715-1717

[5] T. Sizer, R. LaMarche, and T. Woodward, "Point source heating effects in multiple quantum well modulators," Applied Physics Letters, Vol. 61, No. 4, 1992, pp. 420-422

[6] R. Mottahedeh, G. Parry, M. Whitehead, J. Roberts, and C. Button, "High power performance of asymmetric Fabry-Perot MQW modulators," IEEE Photonics Technology Letters, Vol. 6, No. 6, 1994, pp. 703-705

[7] D. Hutchings, C. Park, A. Miller, "Modeling of cross-well carrier transport in a multiple quantum well modulator," Applied Physics Letters, Vol. 59, No. 23, 1991, pp. 3009-3011

[8] A. Fox, D. Miller, G. Livescu, J. Cunningham, J. Henry, and W. Jan, "Exciton saturation in electrically biased quantum wells," Applied Physics Letters, Vol. 57, No. 22, 1990, pp. 2315-2317

[9] T. Wood, J. Pastalan, C. Burrus, B. Johnson, B. Miller, J. deMiguel, U. Koren, and M. Young, "Electric field screening by photogenerated holes in multiple quantum wells: A new mechanism for absorption saturation," Applied Physics Letters, Vol. 57, No. 11, 1990, pp. 1081-1083

[10] M. Watson, J. Chilla, J. Rocca, J. Kim, D. Lile, T. Vogt, and G. Robinson, "Saturation intensity and time response of InGaAs-InGaP MQW optical modulators," IEEE Journal of Quantum Electronics, Vol. 31, No. 2, 1995, pp. 254-260

[11] R. Morgan, L. Chirovsky, M. Focht, R. Leibenguth, "High-power quantum well modulators exploiting resonant tunneling," Applied Physics Letters, Vol. 59, No. 27, 1991, pp. 3524-3526.

[12] T. Woodward, T. Sizer, D. Sivco, and A. Cho, "InGaAs/GaAs multiple quantum well modulators for the 1.02-1.07μm wavelength range," Applied Physics Letters, Vol. 57, 1990, p.548-550

[13] T. Sizer, T. Woodward, U. Keller, K. Sauer, T. Chiu, D. Sivco, A. Cho, "Measurement of carrier escape rates, exciton saturation intensity, and saturation density in electrically biased multiple quantum well modulators," IEEE Journal of Quantum Electronics, Vol. 30, No. 2, 1994, pp. 399-407

[14] S. Nakadate, "Phase detection of equidistant fringes for highly sensitive optical sensing. I. Principle and error analyses," Journal of the Optical Society of America A (Optics and Image Science), Vol. 5, No. 8, 1988, p.1258-1264

[15] C. Fan, B. Mansoorian, D. Van Blerkom, M. Hansen, V. Ozguz, S. Esener, and G. Marsden, " Digital free-space optical interconnections: a comparison of transmitter technologies," Applied Optics, Vol. 34, No. 17, 1995, pp. 3103-3115

[16] K. Goosen, J. Cunningham, M. Santos, and W. Jan, "Measurement of modulation saturation intensity in strain-balanced undefected InGaAs/GaAsP modulators operating at 1.064μm," Applied Physics Letters, Vol. 63, No. 4, 1993, pp. 515-517

[17] C. Barron, C. Mahon, B. Thibeault, G. Wang, W. Jiang, L. Coldren, and J. Bowers, "Milimeter-wave asymmetricFabry-Perot modulators," IEEE Joournal of Quantum Electronics, Vol. 31, No. 8, 1995, pp 1484-1493

[18] S. Nakadate, "High precision retardation measurement using phase detection of Young's fringes," Applied Optics, Vol. 29, No. 2, 1990, pp.242-246

[19] G. Kranzler, J. Moursund, *Statistics for the Terrified*, New Jersey: Prentice Hall, 1995

[20] B. Brown, M. Hollander, *Statistics: A Biomedical Introduction*, New York: Wiley, 1977